

A novel method for calculating the energy barriers for carbon diffusion in ferrite under heterogeneous stress

Deyana S. Tchitchevova,^{1,2} Julien Morthomas,² Fabienne Ribeiro,¹ Roland Ducher,³ and Michel Perez²

¹IRS[N], PSN, SEMIA, LPTM, Saint-Paul-Lez-Durance, France

²Univ. Lyon, INSA Lyon, MATEIS, UMR CNRS 5510, Villeurbanne, France

³IRS[N], PSN, SAG, LETR, Saint-Paul-Lez-Durance, France

(Received 13 January 2014; accepted 30 June 2014; published online 21 July 2014)

A novel method for accurate and efficient evaluation of the change in energy barriers for carbon diffusion in ferrite under heterogeneous stress is introduced. This method, called Linear Combination of Stress States, is based on the knowledge of the effects of simple stresses (uniaxial or shear) on these diffusion barriers. Then, it is assumed that the change in energy barriers under a complex stress can be expressed as a linear combination of these already known simple stress effects. The modifications of energy barriers by either uniaxial traction/compression and shear stress are determined by means of atomistic simulations with the Climbing Image-Nudge Elastic Band method and are stored as a set of functions. The results of this method are compared to the predictions of anisotropic elasticity theory. It is shown that, linear anisotropic elasticity fails to predict the correct energy barrier variation with stress (especially with shear stress) whereas the proposed method provides correct energy barrier variation for stresses up to ~ 3 GPa. This study provides a basis for the development of multiscale models of diffusion under non-uniform stress. © 2014 AIP Publishing LLC. [<http://dx.doi.org/10.1063/1.4889854>]

I. INTRODUCTION

The diffusion of carbon in iron controls the kinetics of many transformations in steels. Cementite precipitation,¹ martensite ageing,² massive austenite \leftrightarrow ferrite transformation,³ and bainite formation⁴ are of major importance for the steel industry.

Diffusion of carbon in defect free ferrite (the body-centered cubic structure of iron) is a fairly well known mechanism: carbon hops from one octahedral site to another passing through a tetrahedral site (the saddle point). The diffusion of carbon in perfect iron has, therefore, been massively studied and characterized (e.g., with mechanical spectroscopy⁵ and Snoek relaxation⁶), leading to a large collection of data on a wide range of temperatures.⁷ However, when other defects are present in iron, carbon may interact with them, thus affecting both the diffusion mechanism and its kinetics. For instance, the high amount of carbon in martensite induces tetragonal distortion of the matrix, which modifies the activation energy, or diffusion energy barrier, of carbon.⁸ Similarly, plastic deformation has been proven to modify carbon diffusion due to the presence of dislocations (pipe diffusion).⁹

The case of dislocations is particularly interesting because they create very large and non-uniform stresses. This heterogeneous stress field induces important effects on the migration energy barrier of impurities and leads to anisotropic diffusion. One example of particular interest is the diffusion and segregation of interstitial carbon atoms to dislocations introduced by plastic deformation in ferritic iron, leading to the growth of so-called Cottrell atmospheres around the dislocations, which is well known to be responsible for static

strain aging in ferritic steels.¹⁰ Interaction between dislocations and interstitial atoms has been studied experimentally by various techniques: e.g., mechanical spectroscopy to get the binding energies,¹¹ thermoelectric power to get the segregation kinetics.¹² However, no experimental technique has ever investigated the local carbon motion around a dislocation. To-mographic atom probe may be one of the most promising techniques for investigating local repartition of carbon around a dislocation. Although an atmosphere has successfully been imaged with this technique,¹³ the associated dislocation itself has never been positively identified.

Atomistic simulation techniques provide a good alternative for studying diffusion processes in the presence of stress. Molecular dynamics (MD) could serve as a perfect framework if it were not so limited in simulation time span (typically, a few ns¹⁴). On the other hand, the atomic Kinetic Monte Carlo (aKMC) method is very well adapted for studying the diffusion of atomic species. For more details on aKMC, see the short introduction of Voter¹⁵ and the comprehensive textbook of Landau and Binder.¹⁶ In aKMC, a system is advanced from one minimum energy configuration to another one by knowing the different escape pathways and the corresponding escape rates. The latter are derived from transition state theory and are functions of the system temperature, energy barrier, and a rate pre-factor (typically about 10^{13} – 10^{14} s⁻¹). If the impact of the stress field induced by the presence of a defect on the rate pre-factors is usually considered as small,¹⁷ it cannot be neglected on the energy barriers.

Therefore, one need to quantitatively account for the energy barrier changes induced by the stress field. Two general

strategies are possible depending on the studied system: the first one is based on the construction of a catalog which is then used by an aKMC algorithm, while the second calculates the energy barriers on-the-fly during the aKMC simulations.

If the stress field is homogeneous, its effect on the energy barriers can be calculated *a priori* with Molecular Statics (MS) using an appropriate interatomic potential, as done by Garruchet and Perez¹⁸ to predict the Snoek relaxation in iron. For more complex stress fields, a kind of brute force method can be employed, where all energy barriers of the system are calculated with MS and stored in an exhaustive catalog. This method has been successfully used in order to predict the segregation kinetics of one carbon atom around a dislocation.¹⁹ This approach relies on the assumption that the system configuration is fixed and will not evolve during the simulation, the latter assumption being clearly wrong when a Cottrell atmosphere is growing up. Other methods are based on comparing actual situation with a catalog using either artificial neural network²⁰ or topological classification of events (NAUTY).²¹ These methods are still under development and should be devoted to complex cases where no other method might work.

Another possibility is to use an adaptive aKMC algorithm where the key step is to recompute on-the-fly the energy barriers for each new generated configuration by using methods to locate the saddle points on the potential energy surface. When both the initial and the final states are known, chain-of-states methods such as the original Nudged Elastic Band (NEB) method^{22,23} or the Doubly Nudged Elastic Band (DNEB) method²⁴ are generally used. By contrast, when only the initial state is known, algorithms such as the Activation-Relaxation Technique (ART),²⁵ ART-*nouveau* (ARTn),^{26,27} or the Dimer method²⁸ are employed. If these approaches are very powerful to search for pathways and characterize them on-the-fly, the benefits of their use come with a high computational cost as compared to the regular aKMC. MD acceleration methods, such as parallel replica dynamics, hyperdynamics, and temperature-accelerated dynamics²⁹ are being developed with large potential applications but still at high computational cost.

Finally, a smart and efficient way to incorporate the effect of stress on diffusion is to use elasticity theory calculations, as recently performed by Subramanian *et al.*¹⁷ This approach requires the knowledge of the local elastic strain interacting with the point defect. It is fast and easy to implement, but is limited to relatively small deformations, where linear elasticity applies. Furthermore, unlike the stress state, which is readily calculated from the interatomic potential (based on the virial theorem), the strain state may be more expensive to obtain, and elasticity relies on its determination.

In this work, we address the effect of a heterogeneous stress field on diffusion energy barriers by presenting an alternative to the above cited approaches. This method, called Linear Combination of Stress States (LinCoSS), is very fast and easy to implement. It is based on (i) the construction of a set of functions giving the energy barrier modification for any kind of simple stress state, and (ii) the linear combination of these functions in order to get the actual stress state. The paper is outlined as follows. Simulation procedures are presented in Sec. II. Then, the three methods for calculating the

energy barriers for carbon diffusion (namely, climbing image nudge elastic band (CI-NEB), elasticity theory, and LinCoSS) are introduced in Sec. III. Finally, in Sec. IV, these three methods are compared, their accuracy is discussed and regions of their validity are established.

II. SIMULATION PROCEDURES

A. Simulation box

The evolution of the diffusion barriers induced by an imposed stress was analyzed by using a supercell of 6750 iron atoms and one carbon atom, with periodic boundary conditions. We verified that this cell size is large enough in order to get rid of border effects on the energy barrier. The iron atoms were arranged on a bcc lattice. In a stress free bcc iron crystal, interstitial carbon is found in an octahedral (o) site, which is located in the middle of one of the three edges of the cubic unit cell (Fig. 1).

Considering the orientation of the two iron atoms that are the first nearest neighbors of the carbon atom, there are three structurally equivalent variants of the octahedral sites with major tetragonal axis directed along [100], [010], or [001] (Fig. 1). These structurally equivalent variants are also energetically equivalent in a stress free state. Obviously, this equivalence is lost when a stress field (internal or applied) is imposed on the crystal. A carbon atom migrates from an octahedral site to one of its four neighboring octahedral sites passing through a saddle point on the potential energy surface. In the stress free crystal, the saddle point coincides with the tetrahedral (t) site located midway between the two octahedral sites. According to harmonic transition state theory, the energy barrier for a transition between adjacent states $i \rightarrow j$ (here, between two octahedral sites) is given by $\Delta E_{i \rightarrow j} = E^t - E_i^o$, where E^t is the total energy of the system at the saddle point (tetrahedral site) and E_i^o is the total energy of the system at the state i (octahedral site).

B. Interatomic potential

The interatomic interactions were described with a Fe-C potential, built according to the Embedded Atom Method (EAM).³⁰ The pure Fe part was developed by Mendelev

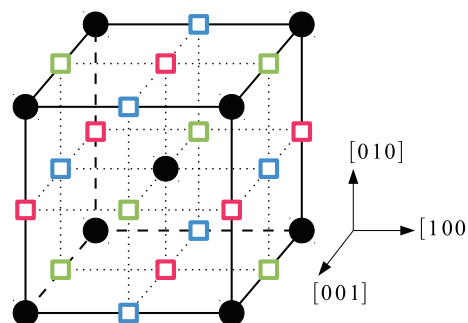


FIG. 1. A schematic illustration of the three different octahedral site positions in the bcc unit cell. The iron atoms are represented by filled black circles. The three structurally equivalent variants of the octahedral sites with major tetragonal axis directed along [100], [010], or [001] are given by the open blue, red, and green squares, respectively. The dotted lines indicate the minimum energy path for carbon migration in the stress free bcc unit cell.

*et al.*³¹ This Fe–C potential was recently modified in order to correct the description of the potential energy landscape around the saddle point.³² The bcc equilibrium lattice parameter at 0 K given by this potential is $a_0 = 0.28553$ nm. Atomistic simulations presented in this work were performed with LAMMPS.³³

C. Box deformation in order to get simple stresses and associated strain tensors

Uniaxial stress was obtained by adjusting the box dimensions L_x , L_y , and L_z in such a way that all stress components except one on the diagonal are zero. Then, the strain tensor ϵ_{ij} can be written as

$$\epsilon_{ii} = \frac{\Delta L_i}{L_i}, \quad \epsilon_{ij} = 0 \text{ for } i \neq j. \quad (1)$$

Shear stress was obtained by imposing a tilt on the simulation box, corresponding to a simple shear deformation. The latter is defined as $\gamma_{ij} = \Delta u_i / L_j$, where Δu_i is the displacement factor along direction i , and L_j is the box length along direction j . Then, all box dimensions L_x , L_y , and L_z were adjusted so as to obtain zero diagonal components of the stress tensor. Thus, the simulation box experiences a pure shear stress. The strain tensor is then given by linear elasticity

$$\epsilon_{ij} = \frac{\gamma_{ij} + \gamma_{ji}}{2}, \quad \epsilon_{ij} = 0 \text{ for } i = j. \quad (2)$$

D. Box under arbitrary homogeneous stress

Arbitrary homogeneous stress states of the stress free simulation box described in Sec. II A were obtained according to the following procedure. Since the stress tensor has 6 independent components, which makes the implementation of a systematic analysis complicated, we choose to vary only those components relevant to a further comparison with the complex heterogeneous stress of an edge dislocation, namely, the σ_{xx} , σ_{yy} , and σ_{xy} components. First, an arbitrary homogeneous deformation (in %) is imposed on the box by varying ϵ_{xx} , ϵ_{yy} in the range [0 : 0.7] with 11 points each, γ_{xy} in the range [0 : 1.5] with 23 points, ϵ_{zz} being fixed at the arbitrary low value of 0.03 %, and γ_{yz} , γ_{xz} at 0.2 %. Thus, a regular grid with 2783 points was generated for each combination of the strain tensor components. Then, the system was allowed to relax the atomic coordinates at constant box volume, and the resulting homogeneous stress is calculated through the virial theorem. The values of the stress field components (in GPa) σ_{xx} , σ_{yy} were generated in the range [0.02 : 2.6], σ_{xy} in the range [0.07 : 1.8], σ_{zz} in the range [0.06 : 1.9], and σ_{yz} , σ_{xz} were about 0.21–0.23 GPa. Although the generated grid is unstructured, the set of points are distributed homogeneously over the range studied. The grid point distribution is shown in Fig. 2, in terms of the hydrostatic (σ_h) and von Mises (σ_v) stresses, calculated as

$$\begin{aligned} 3\sigma_h &= \sigma_{xx} + \sigma_{yy} + \sigma_{zz}, \\ 2\sigma_v^2 &= (\sigma_{xx} - \sigma_{yy})^2 + (\sigma_{yy} - \sigma_{zz})^2 + (\sigma_{xx} - \sigma_{zz})^2 \\ &\quad + 6(\sigma_{xy}^2 + \sigma_{xz}^2 + \sigma_{yz}^2). \end{aligned} \quad (3)$$

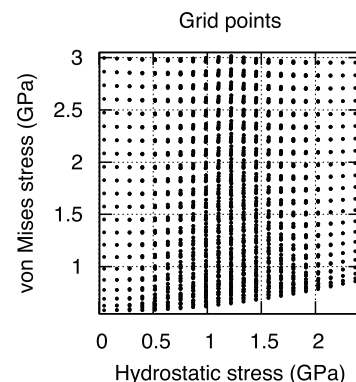


FIG. 2. Distribution of grid points generated for arbitrary homogeneous stress states.

Obviously, the entire range is well represented by the generated points, except for the region of high hydrostatic and very low von Mises stresses. The discussion based on results presented in Sec. IV B demonstrates that this region is not significant to the conclusions of this work.

E. Box with an edge dislocation

The simulation box employed for this part of the present study consisted of a cylinder of radius 15 nm and height 4 nm with an edge dislocation in the center, the dislocation line being parallel to the cylinder axis. Since a dislocation is known to destroy the lattice periodicity in directions perpendicular to its line, periodic boundary conditions were applied only along the dislocation line. Again, the iron atoms (about 200 000) have been arranged on a bcc lattice with $a_0 = 0.28553$ nm, the equilibrium lattice parameter given by the EAM potential used throughout this work. The edge dislocation have been created by displacing the iron atoms according to the anisotropic elasticity theory of straight line defects. The Burgers vector is $\vec{b} = a_0/2[111]$, the glide plane is a $\{\bar{1}01\}$ plane, and the dislocation line is oriented along the $[1\bar{2}\bar{1}]$ direction. Details on how the edge dislocation have been introduced in the simulation box can be found in Ref. 19.

Figure 3 shows the distribution of internal stress around the edge dislocation in terms of hydrostatic (σ_h) and von Mises (σ_v) stresses, given by Eq. (3). Note that local stresses near the dislocation core can reach very high values: more than 3 GPa at distances lower than a few nanometers away from the dislocation line.

III. METHODS FOR CALCULATING DIFFUSION ENERGY BARRIERS

A. Climbing image nudge elastic band

The NEB, originally proposed by Henkelman and Jónsson,²³ is a method for finding saddle points and minimum energy paths between known initial and final state positions. The method works by simultaneous optimization of a chain of intermediate images along the transition path. Each image finds the lowest energy possible while maintaining

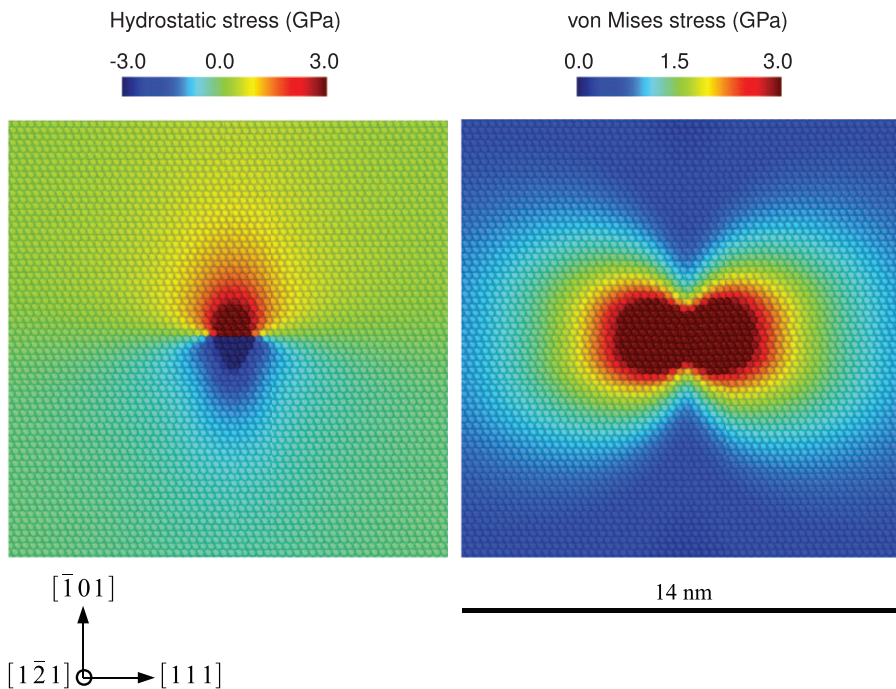


FIG. 3. Atomistic stress distribution of a simulation box containing an edge dislocation in the centre (plot area: $14 \times 14 \text{ nm}^2$): (a) hydrostatic stress and (b) von Mises stress. Atoms are coloured by stress. This figure was created with OVITO software (<http://ovito.org>).³⁴

equal spacing to neighboring images. This constrained optimization is done by adding spring forces along the band between images and by projecting out the component of the force due to the potential perpendicular to the band. The doubly NEB method²⁴ includes a portion of the spring gradient perpendicular to the path. This accelerates the optimization in the early stages, but may inhibit full convergence in the later stages.³⁵ The “doubly-nudged” modification by Trygubenko and Wales²⁴ was found to improve stability for minimization using a quasi-Newton approach with a loose convergence criterion, a procedure designed to produce candidates for subsequent refinement by hybrid eigenvector-following.³⁶

In this paper, we used the CI-NEB implementation in LAMMPS. It serves as a reference method and is used throughout this paper so as to compare the two other methods. Note that the CI-NEB energy barrier calculations are performed at constant volume. Thus, with the Fe–C potential, we obtain a diffusion barrier for carbon migration in a stress free ferrite matrix of $\Delta E^0 = 0.815 \text{ eV}$, in agreement with previous measurements.³²

B. Anisotropic elasticity theory

Within elasticity theory, a point defect is seen as a singular source of stress and modelled by its force moment tensor, P_{ij} , also called “elastic dipole.” As discussed in previous work,³⁷ the tensor P_{ij} can be deduced from atomistic simulations.

The total energy of a periodic simulation box having a volume V , containing a point defect characterized by its elastic dipole P_{ij} , and submitted to a homogeneous strain ϵ_{ij} is

given by³⁸

$$E^{o,t}(\epsilon_{ij}) = E^o(0) - P_{ij}^{o,t} \epsilon_{ij} + \frac{1}{2} V C_{ijkl} \epsilon_{ij} \epsilon_{kl}, \quad (4)$$

where C_{ijkl} are the elastic constants of the host crystal, $P_{ij}^{o,t}$ is the elastic dipole corresponding to octahedral (P_{ij}^o) or tetrahedral (P_{ij}^t) position, and $E^o(0)$ is the energy of the same box containing the point defect without external strain (at $\epsilon = 0$). For brevity, the determination of the dipole tensors is reported in the Appendix.

By using Eq. (4) we can obtain the total energy of the simulation box containing one carbon atom occupying an octahedral or tetrahedral site and experiencing a homogeneous strain. The corresponding energy barrier for carbon migration as a function of strain can be evaluated from the difference of total energy for carbon at minimum and carbon at saddle point

$$\begin{aligned} \Delta E(\epsilon) &= E^t(\epsilon) - E^o(\epsilon) \\ &= E^t(0) - E^o(0) - (P_{ij}^t - P_{ij}^o) \epsilon_{ij} \\ &= \Delta E(0) - (P_{ij}^t - P_{ij}^o) \epsilon_{ij}, \end{aligned} \quad (5)$$

where $\Delta E(0) = 0.815 \text{ eV}$ is the energy barrier for carbon migration in a non-strained iron matrix. The previous expression can also be written as a function of stress

$$\Delta E(\sigma) = \Delta E(0) - (P_{ij}^t - P_{ij}^o) S_{ijkl} \sigma_{kl}, \quad (6)$$

where S_{ijkl} is the compliance tensor.

When the simulation box was submitted to an homogeneous and known strain, Eq. (5) was used in order to get the energy barriers. In the case of unknown and heterogeneous strain (such as the strain induced by a dislocation, see Sec. IV C), Eq. (6) was used instead. Then, the stress

tensor was calculated through the virial theorem at the point of interest. The compliance tensor we used was deduced from the elastic constants obtained for the perfect bcc iron with the EAM potential (the elastic constants corresponding to the potential we used are $C_{11} = 243$, $C_{12} = 145$, and $C_{44} = 116$ GPa; similarly, $S_{11} = 7.429 \times 10^{-12}$, $S_{12} = -2.776 \times 10^{-12}$, and $S_{44} = 8.621 \times 10^{-12}$ Pa $^{-1}$).

C. The LinCoSS method

1. Principle

The LinCoSS method is based on the decomposition of a complex stress state into a linear combination of uniaxial and pure shear stress states. This idea can be simply expressed as follows:

$$\begin{bmatrix} \sigma_{xx} & \sigma_{xy} & \sigma_{xz} \\ \sigma_{yx} & \sigma_{yy} & \sigma_{yz} \\ \sigma_{zx} & \sigma_{zy} & \sigma_{zz} \end{bmatrix} = \begin{bmatrix} \sigma_{xx} & 0 & 0 \\ 0 & 0 & 0 \\ 0 & 0 & 0 \end{bmatrix} + \begin{bmatrix} 0 & 0 & 0 \\ 0 & \sigma_{yy} & 0 \\ 0 & 0 & 0 \end{bmatrix} + \begin{bmatrix} 0 & 0 & 0 \\ 0 & 0 & 0 \\ 0 & 0 & \sigma_{zz} \end{bmatrix} + \begin{bmatrix} 0 & \sigma_{xy} & 0 \\ \sigma_{yx} & 0 & 0 \\ 0 & 0 & 0 \end{bmatrix} + \begin{bmatrix} 0 & 0 & \sigma_{xz} \\ 0 & 0 & 0 \\ \sigma_{zx} & 0 & 0 \end{bmatrix} + \begin{bmatrix} 0 & 0 & 0 \\ 0 & 0 & \sigma_{yz} \\ 0 & \sigma_{zy} & 0 \end{bmatrix}. \quad (7)$$

Therefore, one may assume that the effect of an arbitrary stress field, σ_{ij} , on the energy barriers for impurity migration could be simply evaluated by a linear combination of the effects induced by each stress field component

$$\Delta E(\sigma) = \Delta E(\sigma_{xx}) + \Delta E(\sigma_{yy}) + \Delta E(\sigma_{zz}) + \Delta E(\sigma_{xy}) + \Delta E(\sigma_{xz}) + \Delta E(\sigma_{yz}) - 5\Delta E(0), \quad (8)$$

where $\Delta E(\sigma_{ij})$ are the diffusion energy barriers under uniaxial or pure shear stresses. They can be stored as a set of functions that have the best fit to the series of CI-NEB data points.

2. Fitting procedure

In order to evaluate the functions $\Delta E(\sigma_{ij})$, uniaxial and pure shear stress states were obtained according to the procedures detailed in Sec. II.

a. Uniaxial stress. The evolution of the diffusion barrier when a carbon atom jumps from one octahedral site to an adjacent site as a function of the resulting uniaxial stress is presented in Fig. 4. We show data obtained by CI-NEB calculation for uniaxial stress tests along the [100], [010], and [001] directions (the corresponding tensorial uniaxial stress components are denoted as σ_{xx} , σ_{yy} , and σ_{zz} , respectively), and for two of the six possible migration pathways between the three octahedral variants. However, due to the symmetry of the problem, it is clear that the values of the diffusion barriers for one of the pathways can be used to obtain the values

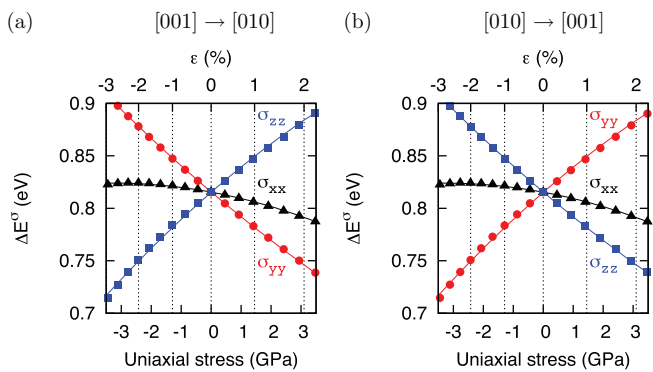


FIG. 4. Carbon diffusion between octahedral variants: (a) from [001] to [010], (b) from [010] to [001]. The black triangles, red circles, and blue squares give data from molecular statics calculations. The corresponding black, red, and blue curves show the fit from Eq. (9) as a function of uniaxial stress along the [100], [010], and [001] directions (the corresponding tensorial uniaxial stress components are denoted as σ_{xx} , σ_{yy} , and σ_{zz} , respectively).

of all possible migration pathways by performing the appropriate permutations.

In Fig. 4(a), the evolution of the diffusion barriers exhibits a nonlinear behaviour for σ_{zz} and σ_{xx} uniaxial stress (blue squares and black triangles, respectively) when going from the [001] to the [010] variant, while a quasi-linear behaviour is observed for σ_{yy} uniaxial stress (red circles). In Fig. 4(b), when carbon migrates from the [010] to the [001] variant, the opposite happens due to the symmetry of the system, i.e., a nonlinear (quasi-linear) evolution of the diffusion barriers is observed for σ_{yy} (σ_{zz}) uniaxial stress. As demonstrated in a previous work,¹⁸ there is an energetically favoured octahedral site depending on the resulting stress (traction or compression), whereas the saddle point energy is relatively insensitive to uniaxial traction. For instance, in the case of σ_{yy} uniaxial stress, the [010] variant is favoured under traction (Fig. 4(b)), while the [001] variant is favoured under compression (Fig. 4(a)). Indeed, the two iron atoms that are the first nearest neighbors of the [010] octahedral variant are moved aside under traction, leaving more space for the carbon atom. However, the energy barrier for carbon diffusion between the [001] and [100] variants when the simulation box is experiencing σ_{xx} uniaxial traction (compression) is slightly decreasing (increasing) because both octahedral variants are disfavoured (favoured). It should be mentioned, that the diffusion barrier in a stress free state reported in our calculations is different from the value found in Ref. 18, which is due to the fact that the EAM potential employed in this work is not exactly the same as the one used in Ref. 18 (for more details, see Ref. 32). This also explains the upward shift in the diffusion barrier values under uniaxial stress for the results reported in Ref. 18.

From this set of data points, fitting functions have been determined

$$\Delta E_{i \rightarrow j}(\sigma_{ii}) = -a_1 \sigma_{ii}^2 + b_1 \sigma_{ii} + \Delta E^0, \quad (9a)$$

$$\Delta E_{j \rightarrow i}(\sigma_{ii}) = a_2 \sigma_{ii}^2 - b_2 \sigma_{ii} + \Delta E^0, \quad (9b)$$

$$\Delta E_{i(j) \rightarrow j(i)}(\sigma_{kk}) = -a_3 \sigma_{kk}^2 - b_3 \sigma_{kk} + \Delta E^0, \quad (9c)$$

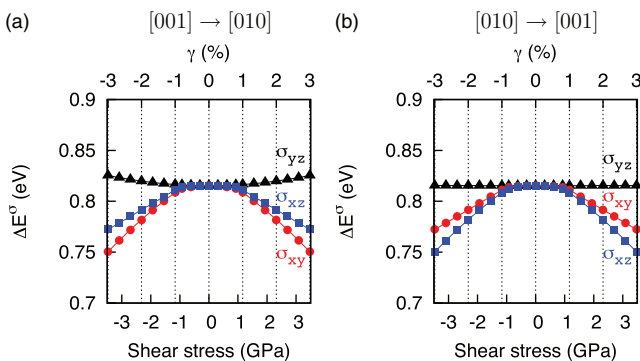


FIG. 5. Carbon diffusion between octahedral variants: (a) from [001] to [010], (b) from [010] to [001]. The black triangles, red circles, and blue squares give data from molecular statics calculations. The black, red and blue curves show the fit from Eqs. (10a) to (10c) as a function of σ_{yz} , σ_{xy} , and σ_{xz} , respectively.

where i , j , and k stand for x , y , or z , and $a_1 = (9.0 \pm 0.1) \times 10^{-4} \text{ eV/GPa}^2$, $a_2 = (6.0 \pm 0.2) \times 10^{-4} \text{ eV/GPa}^2$, $a_3 = (8.0 \pm 0.1) \times 10^{-4} \text{ eV/GPa}^2$, $b_1 = (24.9 \pm 0.2) \times 10^{-3} \text{ eV/GPa}$, $b_2 = (24.3 \pm 0.1) \times 10^{-3} \text{ eV/GPa}$, $b_3 = (5.3 \pm 0.1) \times 10^{-3} \text{ eV/GPa}$, $\Delta E^0 = 0.8153 \pm 0.0003 \text{ eV}$.

Clearly, the energy barrier values can be expanded in a power series in the stress and truncated after the third term (a second-degree polynomial function). The curves given by Eqs. (9) are also shown in Fig. 4, superimposed on the molecular statics data obtained by CI-NEB.

b. Pure shear stress. The energy barriers for interstitial carbon migration were estimated by the CI-NEB method, and their evolution as a function of the shear stress is presented in Fig. 5. We show results for all three shear stress states, and for two of the six possible migration pathways between the three octahedral variants. As explained above, due to the symmetry of the problem, the values of the diffusion barriers for the other possible migration pathways can be obtained by performing the appropriate permutations.

From Fig. 5 it is clear that the plots are symmetric about the $\Delta E(\sigma)$ -axis, which is consistent with the definition of pure shear deformation above. A difference with the uniaxial stress case is the scale on which diffusion barriers evolve when the numerical box experiences uniaxial or pure shear stress. For instance, under uniaxial stress of 1 GPa the diffusion barrier varies by about 25 meV, whereas under pure shear stress of 1 GPa the diffusion barrier varies at the most, depending on the migration pathway, by about 3 meV. We can notice that the σ_{yz} (black triangles) shear stress effect on the diffusion barriers can be neglected. Indeed, the [100] tetrahedral variant is not influenced by the σ_{yz} stress, since the atomic displacement occurs in the [010] direction. By contrast, the diffusion barriers decrease under σ_{xy} (red circles) and σ_{xz} (blue squares) stress states. In these two cases, the displacement field, occurring in the [100] direction, alters the atomic configuration of the carbon at the saddle point in such a way that the total energy of the strained simulation box is decreased, as compared to the reference stress free simulation box.

The functions fitting the data points shown in Fig. 5 were found as follows:

$$\Delta E_{i \rightarrow j}(\sigma_{ij}) = \Delta E_{j \rightarrow i}^{\sigma_{ij}} = \Delta E^0, \quad (10a)$$

$$\Delta E_{k \rightarrow i,j}(\sigma_{ij}) = \begin{cases} -a_4\sigma_{ij}^2 + b_4\sigma_{ij} + c & \text{if } \sigma_{ij} \leq -\sigma', \\ -a_4\sigma_{ij}^2 - b_4\sigma_{ij} + c & \text{if } \sigma_{ij} \geq \sigma', \\ -a_5\sigma_{ij}^2 + \Delta E^0 & \text{elsewhere,} \end{cases} \quad (10b)$$

$$\Delta E_{i,j \rightarrow k}(\sigma_{ij}) = \begin{cases} -a_6\sigma_{ij}^2 + b_5\sigma_{ij} + c & \text{if } \sigma_{ij} \leq -\sigma', \\ -a_6\sigma_{ij}^2 - b_5\sigma_{ij} + c & \text{if } \sigma_{ij} \geq \sigma', \\ -a_7\sigma_{ij}^2 + \Delta E^0 & \text{elsewhere,} \end{cases} \quad (10c)$$

where $a_4 = (2.2 \pm 0.2) \times 10^{-3} \text{ eV/GPa}^2$, $a_5 = (3.5 \pm 0.1) \times 10^{-3} \text{ eV/GPa}^2$, $a_6 = (3.0 \pm 0.3) \times 10^{-4} \text{ eV/GPa}^2$, $a_7 = (1.7 \pm 0.1) \times 10^{-3} \text{ eV/GPa}^2$, $b_4 = (14.5 \pm 0.1) \times 10^{-3} \text{ eV/GPa}$, $b_5 = (15.5 \pm 0.1) \times 10^{-3} \text{ eV/GPa}$, $c = 0.829 \pm 0.002 \text{ eV}$, and $\sigma' = 1.08 \text{ GPa}$.

The fitting curves corresponding to the functions given in Eqs. (10) are presented in Fig. 5, superimposed on the CI-NEB data points.

In summary, the LinCoSS method is based on the knowledge of the functions given in Eqs. (9) and (10) for simple stress states. For an arbitrary stress state, the energy barrier modification can be predicted by using the linear decomposition proposed in Eq. (8). The input parameter of this method is the stress state, readily obtained through the virial theorem in molecular statics/dynamics calculations. In Sec. IV, this method will be validated and compared to elasticity theory predictions.

IV. LINCOSS VS ELASTICITY THEORY

This section is dedicated to the comparison of LinCoSS method predictions with results from elasticity theory for three different cases of increasing complexity. First, elasticity theory is confronted to CI-NEB data for the same uniaxial and pure shear stresses as those used for the calibration of the LinCoSS method (Sec. IV A). Then, elasticity theory and LinCoSS method are compared with CI-NEB for a large number of arbitrary homogeneous stresses (Sec. IV B). Finally, the case of a complex and heterogeneous stress field produced by an edge dislocation (Sec. IV C) is considered in order to analyze the predictions of these three methods and assess their efficiency.

A. Simple homogeneous stress

1. Uniaxial stress states

Figure 6 compares the energy barriers obtained by elasticity theory, Eq. (5), with the CI-NEB data used for the calibration procedure of the LinCoSS method (see Sec. III C 2). A remarkable agreement is observable up to $\sim 1.5\%$ of lattice deformation. Indeed, the absolute error that one should expect by replacing CI-NEB by anisotropic elasticity theory at

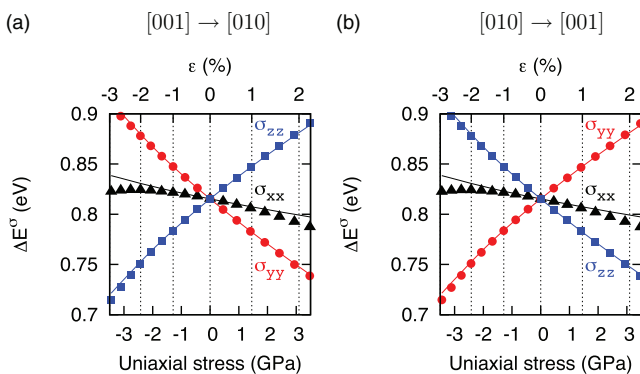


FIG. 6. Energy barriers for carbon diffusion between octahedral variants under uniaxial stress: (a) from [001] to [010], (b) from [010] to [001]. The black, red, and blue curves show the results from Eq. (5) as a function of σ_{xx} , σ_{yy} , and σ_{zz} , respectively. The black triangles, red circles, and blue squares give data from molecular statics calculations.

lattice deformation of $\sim 1.5\%$ vary between 1.5 and 3.5 meV depending on the stress field component σ_{xx} , σ_{yy} , or σ_{zz} , and depending on whether the simulation box is under traction or compression, as well. Obviously, elasticity theory fails to predict the energy barrier evolution as a function of strain when the lattice experiences deformation larger than $\sim 3\%$, since absolute errors higher than 20 meV were obtained.

2. Pure shear stress states

Figure 7 compares the energy barriers obtained by elasticity theory, Eq. (5), with the CI-NEB calculations. As expected, linear elasticity theory predicts no variation of the energy barrier with shear stress. Indeed, the dipole tensor is diagonal while the shear strain tensor is anti-diagonal. In opposition, the CI-NEB method clearly indicates that pure shear affects the energy barriers (Fig. 7). Clearly, linear elasticity theory is inappropriate for evaluating diffusion barrier values when the simulation box is experiencing shear stress corresponding to a lattice deformation higher than $\sim 1\%$. For instance, in the case of σ_{xy} shear stress, the absolute error is ≈ 5 meV at 1% lattice deformation and it climbs quickly above 15 meV at 1.47% lattice deformation.

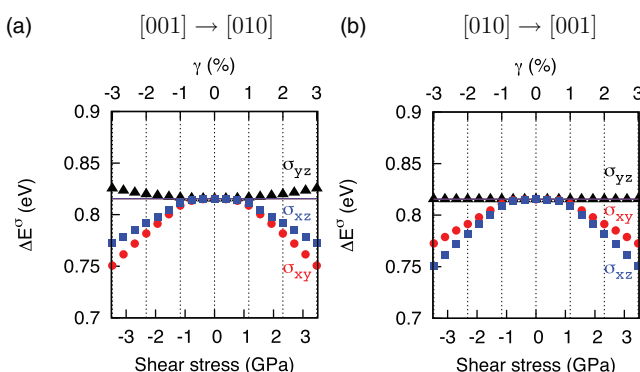


FIG. 7. Energy barriers for carbon diffusion between octahedral variants under shear stress: (a) from [001] to [010], (b) from [010] to [001]. The black, red, and blue curves show the results from Eq. (5) as a function of σ_{yz} , σ_{xy} , and σ_{xz} , respectively. The black triangles, red circles, and blue squares give data from molecular statics calculations.

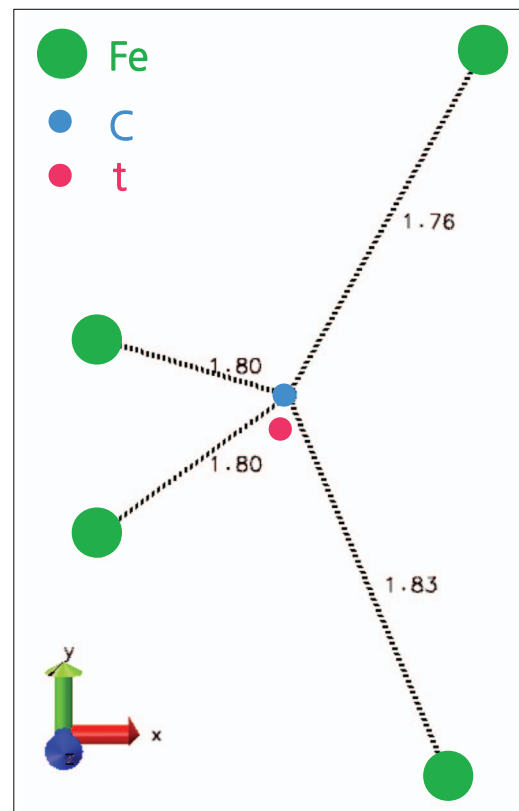


FIG. 8. Atomic positions for Fe (green balls) and for C atom (blue ball) sitting at the saddle point for the case of carbon diffusion in the [100] direction under a uniform shear stress $\sigma_{xy} = 1.7$ GPa, as obtained by the CI-NEB method. The geometrical calculation for the sheared tetrahedron position is also shown (red ball).

By comparing the atomic positions under pure shear stress obtained by CI-NEB calculations for a carbon at the saddle point and for the sheared tetrahedral geometry (Fig. 8), it is obvious that the actual saddle point is located outside the center of mass of the sheared tetrahedron. Thus, when pure shear stress is applied on a bcc crystal, diffusion pathways and saddle point locations cannot be known *a priori*. By contrast, we find that the saddle point is always located midway between the two octahedral sites when the crystal is under uniaxial stress.

From these findings, we can conclude that the large disagreement between elasticity theory and CI-NEB data for the pure shear stress is due to a different saddle point for carbon jump between two octahedral sites than the one assumed to be located at the sheared tetrahedron's center of mass.

B. Complex homogenous stress

We now consider the evolution of interstitial carbon diffusion energies in bcc iron under the effect of an arbitrary homogeneous stress field σ . A large number of combinations of the stress field components were tested in order to establish the validity of our LinCoSS model for evaluating the diffusion barriers. Details on the generated stress states are given in Sec. II D. For the same stress states, we also checked the absolute differences between the diffusion barriers obtained by CI-NEB and elasticity calculations. The relative errors that

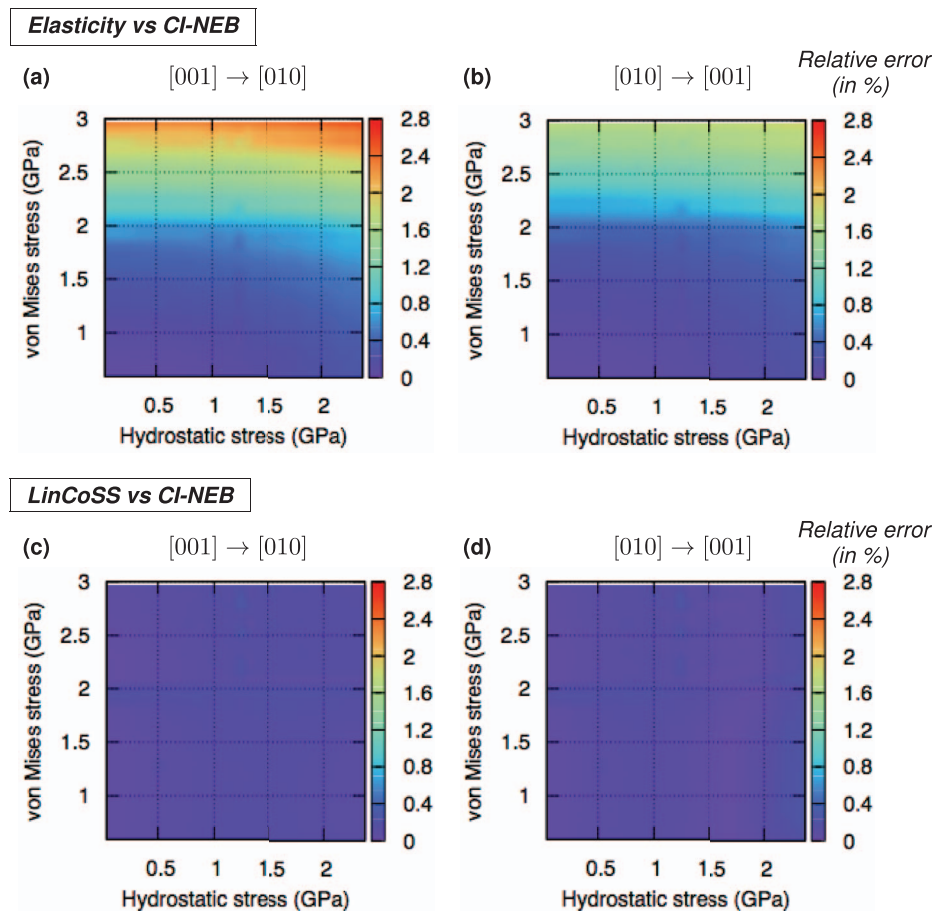


FIG. 9. Relative errors (in %) obtained by Eq. (11), that one should expect when replacing molecular statics CI-NEB by anisotropic elasticity theory (top row) or by LinCoSS method (bottom row) as a function of the hydrostatic and von Mises stresses. Results are based on diffusion barriers for carbon migration between octahedral variants (a) and (c) from [001] to [010]; (b) and (d) from [010] to [001].

one should expect by replacing CI-NEB by linear elasticity theory or by the LinCoSS predictions can be expressed as

$$\eta(\sigma) = \left| \frac{\Delta E^{\text{CI-NEB}}(\sigma) - \Delta E^{\text{ET, LinCoSS}}(\sigma)}{\Delta E^{\text{CI-NEB}}(\sigma)} \right| \times 100, \quad (11)$$

where $\Delta E^{\text{CI-NEB}}(\sigma)$ stands for the diffusion barrier under arbitrary stress calculated by molecular statics with the CI-NEB method, and $\Delta E^{\text{ET, LinCoSS}}(\sigma)$ is the value obtained by either elasticity theory, Eq. (5), or LinCoSS method, Eq. (8).

Since the stress field tensor is composed of six components, which prevents from giving an intuitive graphical representation of the diffusion barrier evolutions, we present the data obtained by Eq. (11) as a function of the hydrostatic (σ_h) and von Mises (σ_v) stresses, see Eq. (3). The corresponding contour plots are shown in Fig. 9 for two of the possible diffusion pathways (see figure caption), those presenting the highest deviations from molecular statics data.

At low von Mises stresses, up to ~ 1 GPa, and hydrostatic stresses up to ~ 3 GPa, very low relative errors (about 0.3%) are predicted both by anisotropic elasticity theory calculations and by the LinCoSS approach. When the von Mises stress is as high as ~ 3 GPa, the relative errors obtained by the LinCoSS approach remain below 0.5% (Figs. 9(c) and 9(d)), still in excellent agreement with the CI-NEB molecular statics calculations. This seems to be the case indepen-

dently of the von Mises stress value in the stress range we studied. On the other hand, at von Mises stresses higher than 1.5 GPa, the relative errors obtained by anisotropic elasticity theory reach almost 3% for some of the diffusion pathways (Fig. 9(a)). This is consistent with the results depicted in Fig. 7, where we have shown that anisotropic elasticity theory fails to predict the correct changes in the diffusion barriers due to a modification of the saddle point position under shear stress.

C. Complex heterogeneous stress

We now consider the carbon diffusion near an edge dislocation in bcc iron. We chose an edge dislocation because it creates a stress field with strong hydrostatic and shear components, by contrast to the stress field of a screw dislocation which is mainly of shear type. The introduction of a dislocation in the simulation box was explained in Sec. II E. Two situations were examined, and the energy barriers for all six possible diffusion pathways were estimated.

First, a carbon atom is diffusing towards the dislocation core near the glide plane of the edge dislocation (Fig. 10), where the von Mises stress increases quickly when the distance to the dislocation core is reduced, as illustrated in Fig. 3(b). For instance, at about $d = 2$ nm the von Mises stress

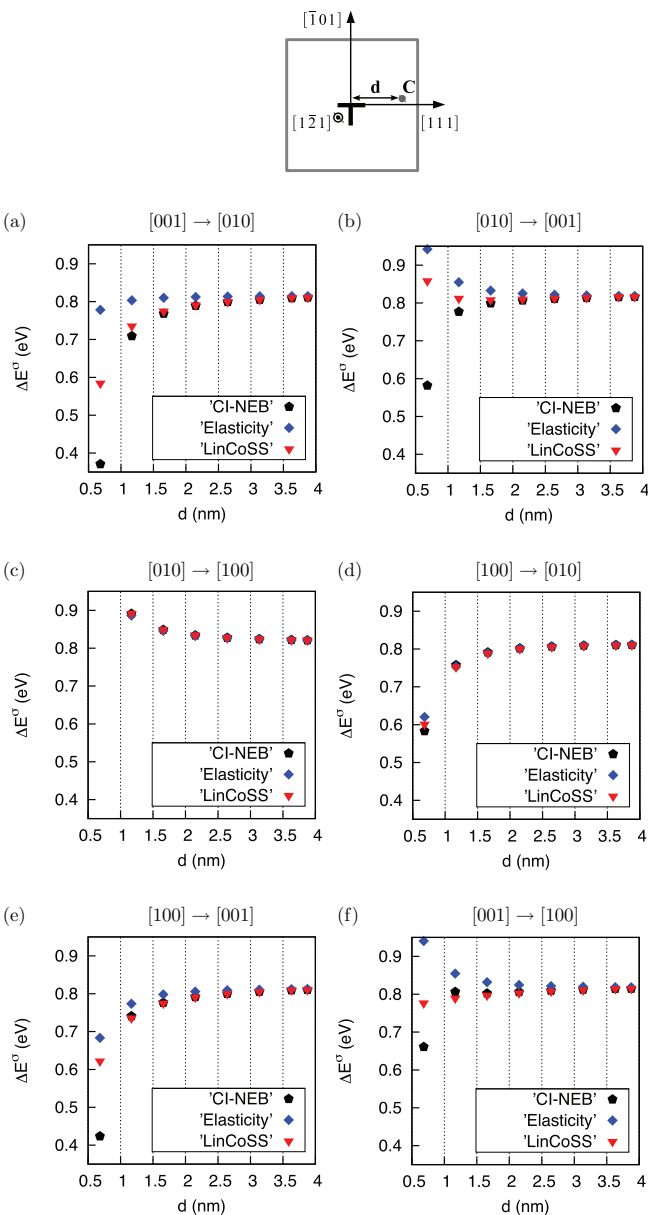


FIG. 10. Top: sketch of a carbon atom diffusing towards the dislocation core near the glide plane of an edge dislocation. (a)–(f) The plots show the evolution of the diffusion energy barriers as a function of the distance to the dislocation line for all six diffusion pathways.

is higher than 3 GPa. Comparison is made between values obtained by the three methods: molecular statics simulations with CI-NEB, elasticity theory, and LinCoSS approach using Eq. (8) in conjunction with the calibrated functions in Eqs. (9) and (10). Figure 10 shows that the LinCoSS method clearly oversteps the limitations of the elasticity theory: at best, the elasticity theory does as well as the LinCoSS method, while for some cases (Figs. 10(b) and 10(f)) it predicts the wrong tendency. The unsatisfactory ability of the elasticity theory in this case is not a surprise since it has been shown to poorly respond to shear stress (see Sec. IV A), which is maximum in the investigated $\{101\}$ plane. Similar discrepancy was observed in Ref. 39, where the authors reported on a comparison between binding energies for a carbon atom occupying an octahedral or a tetrahedral site, calculated by molecular statics

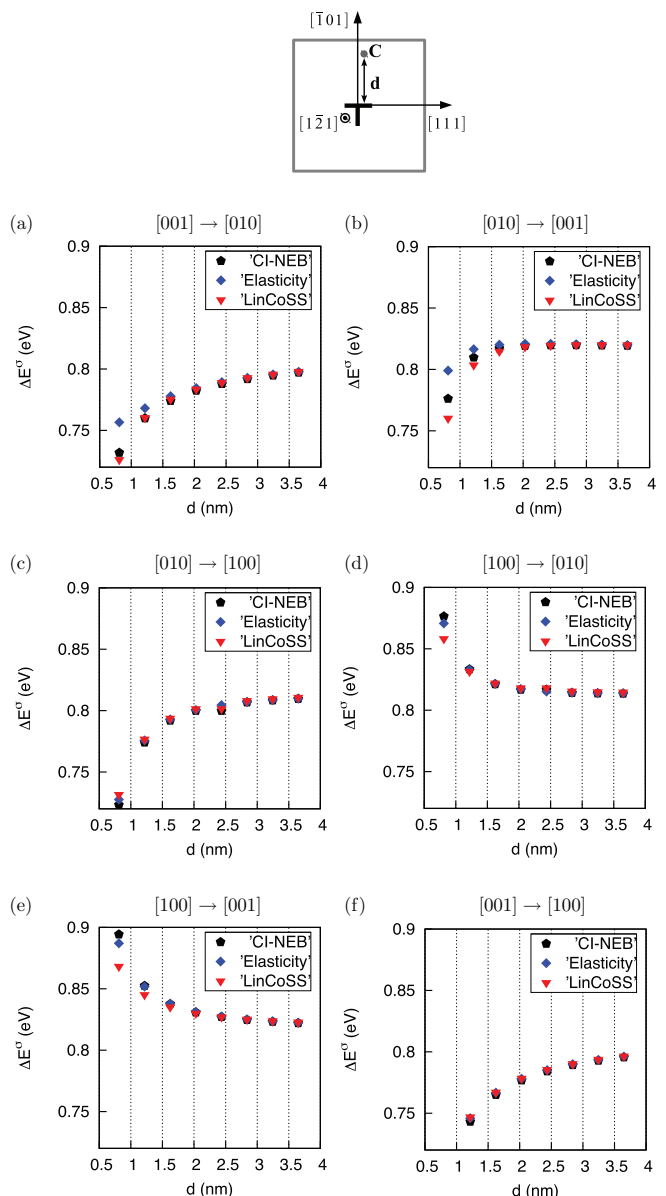


FIG. 11. Top: sketch of a carbon atom diffusing towards the dislocation core along a line perpendicular to the glide plane. (a)–(f) The plots show the evolution of the diffusion energy barriers as a function of the distance to the dislocation line for all six diffusion pathways.

and by elasticity theory. When the carbon is sitting at a tetrahedral site, they found absolute errors higher than 5 meV in the vicinity of the edge dislocation ($\sim 2 - 2.5$ nm), especially near the glide plane (where the σ_{xy} component of the edge dislocation field becomes important¹⁹). On the other hand, the LinCoSS method values are always less than a few meV as compared to the reference CI-NEB data, up to ~ 1 nm from the dislocation line.

Second, a carbon atom is diffusing towards the dislocation core along a line perpendicular to the glide plane of the edge dislocation (Fig. 11), where the hydrostatic stress becomes important in the vicinity of the dislocation core (see Fig. 3(a)). In this case, both elasticity and LinCoSS approach constitute good alternatives to molecular statics calculations, up to ~ 1.2 nm from the dislocation line (Fig. 11).

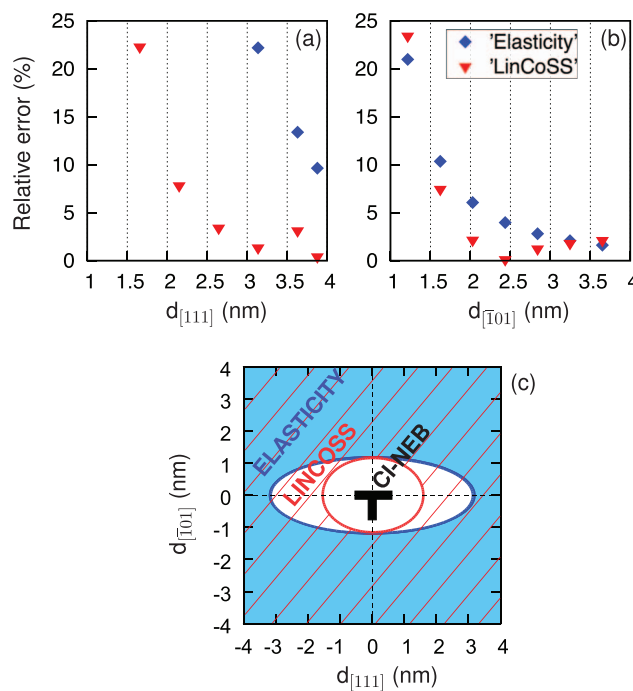


FIG. 12. Top: maximum relative error in the Boltzmann factor (at $T = 400$ K) for carbon diffusing towards the dislocation core (a) near the glide plane, and (b) along a line perpendicular to the glide plane. Bottom: (c) domains of validity of the LinCoSS (red hatched area) and the elasticity (blue area) methods for evaluating the diffusion energy barriers as a function of the local stress developed in the simulation box presented in Fig. 3. The CI-NEB method, used as a reference throughout this work, is valid in the hole box.

In order to summarize all the results obtained for both situations (Figs. 10 and 11), the transition associated with the maximum error (as compared to the reference CI-NEB data) has been determined. The resulting relative errors in the Boltzmann factor, $\exp[-\Delta E(\sigma)/kT]$ (at $T = 400$ K), are shown in Fig. 12 as a function of the distance to the dislocation line, either in the glide plane (shear stress, Fig. 12(a)) or along a line perpendicular to the glide plane (hydrostatic stress, Fig. 12(b)). As it can be seen from Fig. 12(a), the LinCoSS approach constitutes a better approximation to the diffusion barriers, and relative errors of $\sim 20\%$ at $d = 1.6$ nm are achieved when estimating the Boltzmann factors $\exp[-\Delta E(\sigma)/kT]$ (red triangles in Fig. 12(a)). When using elasticity theory, the relative errors in the Boltzmann factors quickly rise above 20% even at distances as far as 3 nm from the dislocation core (blue diamonds in Fig. 12(a)).

Finally, the domain of validity of each method is represented in Fig. 12(c). This domain is limited by the maximum accepted relative error in the Boltzmann factor (i.e., $\sim 20\%$ is a reasonable value): areas delimited by the two ellipses show the regions where the anisotropic elasticity theory and the LinCoSS method shall induce important relative errors in the values of the Boltzmann factors.

Defining the range of validity of each approach is a key parameter if one would want to couple either the elasticity theory or the LinCoSS method to a Monte Carlo scheme. For instance, such coupling between elasticity theory and Monte Carlo is presented in the recent contribution of Subramanian *et al.*,¹⁷ where the strain field has to be known *a priori*. In this

work, we claim that the coupling of a Monte Carlo algorithm with the LinCoSS method would be more versatile since the strain field is not required. Only the stress state is necessary, and it is easily obtained through virial theorem MS/MD calculations, as long as the system can be accurately described by an appropriate interatomic potential.

V. CONCLUSIONS

In this paper, we proposed a novel method, called LinCoSS for Linear Combination of Stress States, for determining the energy barriers for carbon diffusion under heterogeneous stress field. The presence of an imposed (applied or internal) stress field modifies the energy barriers for carbon diffusion because stress influences the energy and the atomic configurations of both the stable position (octahedral site) and the saddle point position (tetrahedral site).

The LinCoSS method is based on a two-stage approach: (i) the effect of a simple stress state (uniaxial stress and pure shear stress) on energy barriers is evaluated for any kind of carbon transition and any kind of simple stress state. Resulting energy barrier modifications are calibrated via specific functions; (ii) it is assumed that the effect of a complex stress state on energy barriers is the sum of the effects of simple stress states composing the complex stress state. Thanks to stages (i) and (ii), the energy barrier evaluation is performed by a simple stress state measurement, which is straightforward in any kind of molecular statics/dynamics packages.

The hypothesis the LinCoSS method is based on has been verified by comparing the resulting energy barriers to brute force CI-NEB measurements for many different complex stress states. It has been demonstrated that the LinCoSS method is very accurate up to relatively high stresses (a few GPa). Furthermore, the LinCoSS method is more accurate than elasticity theory since it provides a better description of the effect of pure shear stress on the energy barriers. In particular, it has been shown that pure shear displaces the saddle point position so that it is no longer located at the tetrahedral site. This latter point is not accounted for in elasticity theory since the impurity elastic dipole is usually obtained from bulk calculations.

Finally, the LinCoSS method has been used in order to predict the energy barriers in the vicinity of an edge dislocation in bcc iron. This method can be readily applied to study carbon diffusion in the presence of one (or several) dislocation, up to a distance as close as ~ 1.6 nm from the dislocation line. The LinCoSS method, coupled to a MC algorithm, could serve as a good framework for modelling carbon diffusion in bcc iron in the presence of any kind of defect (dislocation, vacancy, grain boundary, precipitates, etc.) provided that the stress field induced by the defect does not overpass 3–4 GPa. It is worth noting that it could also be generalized to the case of vacancy diffusion or to the diffusion of other substitutional atoms.

ACKNOWLEDGMENTS

This work was granted access to the HPC resources of the FLMSN, “Fédération Lyonnaise de Modélisation et Sciences

Numériques,” partner of EQUIPEX EQUIP@MESO. The authors also thank Professor C.W. Sinclair (University of British Columbia), Dr. E. Clouet (CEA-Saclay), Professor C. Becquart (Université Lille 1), Professor P. Maugis (IM2NP), and Dr. R. Dubourg (IRSN-Cadarache) for fruitful discussions.

APPENDIX: DETERMINATION OF DIPOLE TENSORS

In order to get the elastic dipole tensors, the same procedure as in Ref. 39 was followed. A single carbon atom was introduced in an octahedral (or tetrahedral) site in a fully periodic simulation box with fixed volume, V . The stress tensor at zero deformation is given by

$$\sigma_{ij} = \frac{1}{V} \left. \frac{\partial E}{\partial \epsilon_{ij}} \right|_{\epsilon=0} = -\frac{1}{V} P_{ij}. \quad (\text{A1})$$

After full coordinate optimization (with a conjugate gradient minimization procedure), the measure of the stress tensor as a function of the box volume gives direct access to the dipole tensor.

Considering that both the octahedral and tetrahedral interstitial sites in stress free bcc crystals have a tetragonal symmetry (the tetragonal axis defines the variant type), the force moment tensor corresponding to a carbon atom is diagonal with only two different diagonal terms. Therefore, values calculated for a [100] octahedral variant are $P_{xx}^o = 8.03$ eV and $P_{yy}^o = P_{zz}^o = 3.40$ eV; for the other two octahedral variants the P_{ii} components are obtained by performing the appropriate permutations. Similarly, for a [100] tetrahedral variant we find $P_{xx}^t = 4.87$ eV for the component along the tetragonal axis and $P_{yy}^t = P_{zz}^t = 6.66$ eV for the other two components.

- ¹D. A. Porter and K. E. Easterling, *Phase Transformation in Metals and Alloys* (Chapman and Hall, London, 1992), p. 514.
- ²K. A. Taylor and M. Cohen, “Ageing of ferrous martensites,” *Prog. Mater. Sci.* **36**, 225–272 (1992).
- ³M. Hillert, “Diffusion and interface control of reactions in alloys,” *Metall. Mater. Trans. A* **6**, 5–19 (1975).
- ⁴H. K. D. H. Bhadeshia, *Bainite in Steels*, 2nd ed. (Institute of Materials, 2001).
- ⁵M. Weller, “Point defect relaxations,” *Mechanical Spectroscopy Q⁻¹* (Trans Tech Pub., 2001), p. 683.
- ⁶J. L. Snoek, “Effect of small quantities of carbon and nitrogen on the elastic and plastic properties of iron,” *Physica* **8**(7), 711–733 (1941).
- ⁷M. Weller, “Anelastic relaxation of point defects in cubic crystals,” *J. Phys. IV* **6**(C8), 63 (1996).
- ⁸M. Hillert, “The kinetics of the first stage of tempering,” *Acta Metall.* **7**(10), 653–658 (1959).
- ⁹M. Cohen, “Self-diffusion during plastic deformation,” *Trans. JIM* **11**, 145–151 (1970).
- ¹⁰A. Cottrell and B. Bilby, “Dislocation theory of yielding and strain ageing of iron,” *Proc. Phys. Soc. A* **62**, 49–62 (1949).
- ¹¹K. Kamber, D. Keeler, and C. Wert, “Interactions of interstitials with dislocations in iron,” *Acta Metall.* **9**, 403–414 (1961).
- ¹²V. Massardier, N. Lavaire, M. Soler, and J. Merlin, “Comparison of the evaluation of the carbon content in solid solution in extra-mild steels by thermoelectric power and by internal friction,” *Scr. Mater.* **50**, 1435–1439 (2004).
- ¹³M. Miller, E. Kenik, K. Russell, L. Heatherly, D. Hoelzer, and P. Maziasz, “Atom probe tomography of nanoscale particles in ODS ferritic alloys,” *Mater. Sci. Eng. A* **353**(1–2), 140–145 (2003).

- ¹⁴D. Frenkel and B. Smit, *Understanding Molecular Simulations: From Algorithms to Applications* (Academic Press, 2002).
- ¹⁵A. F. Voter, “Introduction to kinetic Monte-Carlo,” in *Radiation Effects in Solids*, NATO Science Series Vol. 235, edited by K. E. Sickafus, E. A. Kotomin, and B. P. Uberuaga (Springer, Netherlands, 2007), pp. 1–23.
- ¹⁶D. P. Landau and K. Binder, *A Guide to Monte-Carlo Simulations in Statistical Physics* (Cambridge University Press, Cambridge, England, 2005).
- ¹⁷G. Subramanian, D. Perez, B. P. Uberuaga, C. N. Tomé, and A. F. Voter, “Method to account for arbitrary strains in kinetic Monte-Carlo simulations,” *Phys. Rev. B* **87**, 144107 (2013).
- ¹⁸S. Garruchet and M. Perez, “Modeling the Snoek peak by coupling molecular dynamics and kinetic Monte-Carlo methods,” *Comput. Mater. Sci.* **43**, 286–292 (2008).
- ¹⁹R. G. A. Veiga, M. Perez, C. S. Becquart, C. Domain, and S. Garruchet, “Effect of the stress field of an edge dislocation on carbon diffusion in α -iron: Coupling molecular statics and atomistic kinetic Monte Carlo,” *Phys. Rev. B* **82**, 054103 (2010).
- ²⁰N. Castin and L. Malerba, “Calculation of proper energy barriers for atomistic kinetic Monte Carlo simulations on rigid lattice with chemical and strain field long-range effects using artificial neural networks,” *J. Chem. Phys.* **132**, 074507 (2010).
- ²¹L. K. Béland, P. Brommer, F. El-Mellouhi, J. F. Joly, and N. Mousseau, “Kinetic activation-relaxation technique,” *Phys. Rev. E* **84**, 046704 (2011).
- ²²G. Henkelman and H. Jónsson, “Improved tangent estimate in the nudged elastic band method for finding minimum energy paths and saddle points,” *J. Chem. Phys.* **113**, 9978 (2000).
- ²³G. Henkelman, B. Uberuaga, and H. Jónsson, “A climbing image nudged elastic band method for finding saddle points and minimum energy paths,” *J. Chem. Phys.* **113**, 9901 (2000).
- ²⁴S. A. Trygubenko and D. J. Wales, “A doubly nudged elastic band method for finding transition states,” *J. Chem. Phys.* **120**, 2082 (2004).
- ²⁵G. T. Barkema and N. Mousseau, “Event-based relaxation of continuous disordered systems,” *Phys. Rev. Lett.* **77**, 4358 (1996).
- ²⁶N. Mousseau and G. Barkema, “Traveling through potential energy landscapes of disordered materials: The activation-relaxation technique,” *Phys. Rev. E* **57**, 2419 (1998).
- ²⁷N. Mousseau and G. Barkema, “Activated mechanisms in amorphous silicon: An activation-relaxation-technique study,” *Phys. Rev. B* **61**, 1898–1906 (2000).
- ²⁸G. Henkelman and H. Jónsson, “A dimer method for finding saddle points on high dimensional potential surfaces using only first derivatives,” *J. Chem. Phys.* **111**, 7010–7022 (1999).
- ²⁹A. Voter, F. Montalenti, and T. C. Germann, “Extending the time scale in atomistic simulation of materials,” *Annu. Rev. Mater. Res.* **32**, 321–346 (2002).
- ³⁰C. S. Becquart, J. M. Raulot, G. Beneteux, C. Domain, M. Perez, and S. Garruchet, “Atomistic modeling of an Fe system with a small concentration of C,” *Comput. Mater. Sci.* **40**, 119 (2007).
- ³¹M. I. Mendelev, D. J. Srolovitz, S. Han, A. V. Barashev, and G. J. Ackland, “Development of an interatomic potential for phosphorus impurities in α -iron,” *J. Phys.: Condens. Matter* **16**, S2629–S2642 (2004).
- ³²R. G. A. Veiga, C. S. Becquart, and M. Perez, “Comments on ‘Atomistic modeling of an Fe system with a small concentration of C,’” *Comput. Mater. Sci.* **82**, 118–121 (2014).
- ³³S. Plimpton, “Fast parallel algorithms for short-range molecular dynamics,” *J. Comput. Phys.* **117**, 1–19 (1995).
- ³⁴A. Stukowski, “Visualization and analysis of atomistic simulation data with OVITO – The Open Visualization Tool,” *Model. Simul. Mater. Sci. Eng.* **18**, 015012 (2010).
- ³⁵D. Sheppard, R. Terrell, and G. Henkelman, “Optimization methods for finding minimum energy paths,” *J. Chem. Phys.* **128**, 134106 (2008).
- ³⁶L. J. Munro and D. J. Wales, “Defect migration in crystalline silicon,” *Phys. Rev. B* **59**, 3969 (1999).
- ³⁷E. Clouet, S. Garruchet, H. Nguyen, M. Perez, and C. Becquart, “Dislocation interaction with C in α -Fe: A comparison between atomic simulations and elasticity theory,” *Acta Mater.* **56**, 3450 (2008).
- ³⁸D. J. Bacon, D. M. Barnett, and R. O. Scattergood, “Anisotropic continuum theory of lattice defects,” *Prog. Mater. Sci.* **23**(2–4), 51–262 (1980).
- ³⁹R. G. A. Veiga, M. Perez, C. S. Becquart, E. Clouet, and C. Domain, “Comparison of atomistic and elasticity approaches for carbon diffusion near line defects in α -iron,” *Acta Mater.* **59**, 6963 (2011).